Raman spectral histopathology: towards unsupervised evaluation of tumour resection margins

Kenny Kong[1], Christopher J. Rowlands[1], Adrian Ghita[1], Sundeep Varma[2], William Perkins[2], Iain H. Leach[3], Alexey A. Koloydenko[4], Hywel Williams[5] and Ioan Notingher[1*]

[1] *School of Physics and Astronomy, University of Nottingham, University Park, Nottingham, NG7 2RD, United Kingdom.*

[2] *Dermatology Department, Nottingham University Hospital NHS Trust, QMC Campus, Derby Road, Nottingham, NG7 2UH, United Kingdom.*

[3] *Histopathology Department, Nottingham University Hospital NHS Trust, QMC Campus, Derby Road, Nottingham, NG7 2UH, United Kingdom.*

[4] *Mathematics Department, Royal Holloway, University of London, Egham, TW20 0EX, United Kingdom.*

[5] *Centre of Evidence-Based Dermatology, C Floor South Block, Nottingham University Hospital NHS Trust, QMC Campus, Derby Road, NG7 2UH, United Kingdom.*

Running title: Raman spectral histopatology of skin

Keywords: Raman spectroscopy, Basal cell carcinoma, histopathology, classification, diagnosis, Mohs micrographic surgery.

**Corresponding author:Ioan Notingher, ioan.notingher@nottingham.ac.uk, Tel: +44(0) 11595 15172, fax: +44(0)1159515180.*

Financial support:

Word count: 4656; Figures: 6; Tables: 1.

ABSTRACT

Intra-operative evaluation of resection margins remains a challenge in the surgery of many cancer types. In this study we show that Raman micro-spectroscopy combined with multivariate analysis methods can be used for objective diagnosis of basal cell carcinoma (BCC) in tissue layers excised during Mohs micrographic surgery (MMS). A key feature of this technique is that objective diagnosis can be achieved without tissue sectioning or other preparation procedures. A classification model based on Raman spectra collected from skin samples (65 patients) achieved 90±4% sensitivity and 97±3% in a cross-validation algorithm. This classification model was based on spectral differences originating from the intrinsic differences in chemical composition of the tissue structures. The classification model was used to provide an unsupervised diagnosis of tissue samples containing BCC, including nodular, superficial and infiltrative subtypes, as well as BCC-free samples. In all cases, an excellent agreement between the spectral diagnosis and the gold-standard histopathology was achieved. BCC regions were detected in all tissue samples containing BCC, including infiltrative BCC as small as 40×40 μm^2. Although we showed that the use of selective sampling allows the diagnosis of BCC within 30 minutes, the integration of the spectral models with faster Raman spectroscopic techniques may reduce the imaging times to few minutes, which would be suitable for intra-operative evaluation of tumour margins. While the focus of this study was on diagnosis of BCC during MMS, this is a generic technique which could be potentially developed for use during tissue-conserving surgery for other tissue types.

INTRODUCTION

In tissue-conserving surgery sequential layers of tissues are excised to ensure the removal of all tumour cells while maintaining as much healthy tissue as possible. Negative margins (in which all cancerous cells are removed) have been directly associated with lower local recurrence rates in many cancer types [1]. Conservation of healthy tissue is important for tissue function preservation, would healing and cosmesis. However, identifying the tumour margins intra-operatively remains one of the key challenges in tissue-conserving surgery.

Histopathology is the gold-standard method for evaluation of tissues for many diseases, including cancer. The staining of thin tissue sections (thickness ~10 μm) with various contrast enhancing chemicals followed by examination under an optical microscope allows the discrimination of tissue structures and identification of the tumours. Thus, histopathology is an invaluable tool for evaluating the tumour resection margins during tissue-conserving surgery. For example, Mohs micrographic surgery (MMS) for the treatment of basal cell carcinoma (BCC), which is the focus of this study, relies on the removal of sequential tissue layers which are evaluated during surgery by frozen section histopathology. If the pathologic evaluation during MMS indicates tumour persistence, the location of the tumour is recorded and further tissue removal is performed by the surgeon. BCC is a major health problem as it accounts for ~75 % of skin cancer cases worldwide with more than 60,000 cases being diagnosed each year in the UK [2,3]. Although BCC rarely spreads to distant sites in the body, these cancers can lead to significant tissue destruction and dysfunction. Some BCCs have higher risks of recurrence (43% for regions near the eye and 33% for superior orbital rim and brow [4]), which lead to more aggressive recurrent BCCs. If the treatment option were selected based on lowest recurrence rate, it has been argued that MMS would be chosen for every BCC [4, 5]. It has been shown that the 5-year recurrence rates for BCC treated by MMS are 1.4%-2.5% for primary and 2.4%-4% for recurrent BCC [5-8], significantly lower

than for standard excision (3.2%-10% for primary and 12.1%-17% for recurrent BCC) [7,8]. However, the high costs and time-consuming procedures associated with the current histopathology technique relying on tissue sectioning and staining make it impractical for use during surgery. Therefore intra-operative evaluation of tumour margins is currently carried out only in the treatment of a relatively low number of cancer types, despite the potential benefit to patients.

Apart from being time-consuming, histopathology can only provide a qualitative evaluation of tissues and often suffers from variability due to variations in sample preparation protocols and pathologists' expertise, as well as their ability to maintain their expertise during the examination of a large number of specimens [9,10]. In the case of BCC, a study on 48 samples evaluated by 20 pathologists concluded that the mean sensitivity for detection of BCC was 87% and the specificity was 94% [11]. Immunostaining based on the Ber-ep4 antibody is another method for diagnosis and imaging of BCC [12-14]. However, this marker also attaches to the hair follicles and to sweat glands, which reduces the specificity of this method [13].

Recently, Raman spectroscopy has emerged as a powerful technique for the diagnosis of cancers and imaging of tumours. Raman hand-held probes based on fibre optics have already been used for intra-operative evaluation of tumour margins [15] as well as for guided biopsy [16]. Spectral imaging based on Raman microscopic techniques has the advantage of containing both the morphological and chemical information at a high spatial resolution suitable for the detection of small tumours. Alterations in the molecular properties of tissues during tumour growth provide the additional quantifiable information which can be used for objective diagnosis. Raman microscopy techniques have been used for imaging tumours within thin tissue sections (10-20 μm thickness) and multivariate statistical models had been developed for providing accurate diagnosis (typical sensitivities and specificities higher than

95%) for a wide range of tissues, including skin [17,18], oesophagus [19], prostate [20] and breast [21]. While these studies demonstrated the potential for using Raman microscopy for both imaging and unsupervised diagnosis of tumours, the work reported so far has been limited to tissue sections.

In this study, we demonstrate that accurate evaluation of tumour margins can be achieved by direct analysis of the tissue layers and blocks excised during surgery without requiring sectioning or other sample preparation protocols. Therefore, this approach could represent a considerable advantage as the time-consuming procedures of tissue sectioning and staining could be eliminated. The focus of this study is on Mohs micrographic surgery for the treatment of BCC. Tumour location and accurate diagnosis of BCC (nodular, superficial and infiltrative) was achieved by the unsupervised use of multivariate classification models developed *a priori* through measurements on tissue samples from 65 patients. Therefore, the development of automated "Raman spectral histopathology" which uses simultaneously the morphological and chemical information of tissues without requiring sectioning or other preparation procedures has the potential to advance the surgery by providing an objective diagnosis of all tissue layers.

MATERIALS AND METHODS

2.1 Patients and skin tissue samples

All skin tissue samples were obtained during routine MMS at the Nottingham University Hospitals National Health Service (NHS) Trust. Ethical approval was granted from Nottingham Research Ethics Committee (07/H0408/172) and consent was obtained from all patients. The samples were kept frozen at -20˚C until used for Raman spectral measurements. 'Tissue block' refers to tissue layers thicker than 0.5 mm as removed during MMS. 'Tissue sections' represent skin sections of 20 μm thickness cut from tissue blocks with a microtome (CM 1900 UV, Leica). After the Raman spectroscopy measurements, the analysed skin sections were stained by haematoxylin and eosin (H&E) and the diagnosis was provided by a consultant histopathologist. For tissue blocks, the diagnosis was based on adjacent H&E stained tissue sections.

2.2 Raman micro-spectrometers

The Raman spectra were recorded by two researchers on two custom-built Raman micro-spectrometers based on inverted optical microscopes, 785nm lasers, optimised detectors (DU401-A-BR-DD, Andor Technology) and automated sample stages (H107 controlled by Proscan II controller, Prior Scientific). In this way, the effect of inter-instrument and inter-operator variability on the classification models could be estimated. One instrument consisted of an Eclipse-Ti Nikon inverted optical microscope with a Leica 50×/0.55 objective, Starbright XM Torsana laser and a 77200 Oriel spectrograph. The second instrument comprised a IX71 Olympus optical microscope with a Nikon 50×/0.75 objective, Toptica Xtra laser and a Shamrock 303i Andor spectrograph. The acquisition time for the Raman measurements was 1 or 2 seconds per position and the laser power on the sample surfaces was 100 mW for tissue sections and 300 mW for tissue blocks. The spectrometers were

calibrated using naphthalene and 1,4-Bis(2-methylstyryl) benzene samples (both from Sigma-Aldrich, UK) to an accuracy of 0.5 cm^{-1}.

2.3 Development of the spectral classification models

Raman spectral maps were recorded from skin tissue sections deposited on MgF_2 discs by raster scanning over areas of 1×1 mm^2 in 10 μm steps. The following pre-processing procedures were applied to all Raman spectra: removal of cosmic-ray peaks, subtraction of the background Raman signal of the microscope objective and MgF_2 substrate, subtraction of a baseline based on a rubber band method (the rubber bands were chosen for the profile of the tissue spectrum between the regions of 750-850, 855-950, 951-1050, 1135-1254, 1488-1600, 1675-1750 cm^{-1}), normalisation to zero mean and unit standard deviation [22, 23].

After the Raman measurements, each tissue section was H&E stained and the tissue structures (BCC, epidermis, hair follicle, dermis, inflamed dermis, muscle, sebaceous glands and fat) were identified by a consultant histopathologist. For each spectral map a 3×3 moving average filter was applied and followed by *k*-means clustering to produce a Raman spectral image of the tissue. The number of clusters, *k*, was initially set to 8, and the *k*-means algorithm was applied a second time but only on the spectra corresponding to the clusters which consisted of more than one skin structural class. The pseudo-colour spectral images obtained by this hierarchical application of the *k*-means algorithm were correlated with the tissue structures revealed by the H&E images. The centroid spectra of every cluster containing at least 10 measuring sites were included in the database and labelled as BCC, epidermis and hair follicle, dermis, inflamed dermis, muscle, sebaceous glands and fat. A maximum of 5 centroid spectra per class per patient were included in the database.

The total number of Raman spectra in the database was 703 (374 from one instrument and 329 from the second instrument) and were recorded from tissue samples from 65 patients.

The database included 220 spectra of BCC, 165 of epidermis (combined with hair follicles), 34 of inflamed dermis, 198 of dermis, 22 of fat, 35 of sebaceous glands and 29 of muscle.

2.4 Spectral imaging and automatic diagnosis of tissue sections and blocks

For tissue sections, the sample preparation was the same as that for building the database (Section 2.3). Tissue blocks were deposited on MgF_2 coverslip (0.17mm thick) and were maintained in phosphate buffer saline (PBS) during the measurements. The Raman spectra from a selected region of the tissue were acquired at 10 or 20 μm steps with 2 second integration time at each position. After RMS measurements, all spectra were pre-processed, as discussed in Section 2.3.

Spectral images for both tissue sections and blocks obtained from new patients were obtained using the following method. An initial unsupervised two-step *k*-means clustering algorithm (*k* =30) was used to identify the tissue regions with similar Raman spectra. The classification of each tissue structure in the Raman image was obtained by applying the classification model to the centroid spectrum of each cluster [17, 24, 25].

2.5 Spectral imaging and automatic diagnosis of tissue blocks by selective scanning

A recently developed technique for selective scanning [26] was applied to increase the acquisition speed for the Raman spectral images. The sampling points were determined in real-time by calculating the scores of the LDA classification model corresponding to each Raman spectrum. The LDA model was modified to return a score of 1 for the BCC and epidermis aggregate class and null scores for the other classes. From the real-time classification scores, two interpolated surfaces (nearest neighbour and bicubic spline interpolants) were computed. The next sampling point was located at the sample position for which the difference between the interpolated values was the largest. The final image and

classification of BCC and the skin structures was obtained by applying original LDA model at the end of the measurement, followed by the nearest neighbour method to reconstruct a full interpolated image.

3. RESULTS AND DISCUSSION

3.1 Development of the spectral classification model

The first step in the development of the spectral classification model was to establish a method to assign the measured Raman spectra to the correct tissue structures in the skin samples. This method was based on a supervised process in which the step-wise *k*-means clustering technique was used to provide pseudo-colour images which were then compared to the H&E images. Figure 1A shows a typical example of a skin tissue containing nodular BCC, hair follicles and regions of healthy and inflamed dermis. An initial use of the *k*-means algorithms using eight clusters provided a pseudo-colour image (Figure 1B) which clearly distinguished the healthy dermis regions, oil glands and the hair shafts. However, the BCC regions, hair follicles and the regions of inflamed dermis were all included in the same cluster (coloured red). Figure 1C presents the pseudo-colour image obtained by applying a second supervised step-wise *k*-means algorithm on only the Raman spectra contained in the red cluster in Figure 1B. This method achieved a very good discrimination of the BCC, hair follicles and inflamed dermis as these structures are separated into distinct clusters. Only the centroid spectra from the correctly-identified clustered regions (when compared to the H&E image) were included in the database.

Figure 2 presents the mean of the Raman spectra corresponding to all classes: BCC, epidermis, hair follicles, inflamed dermis, dermis, fat, sebaceous gland and muscle. The assignment of the bands in the Raman spectra has already been established [27]. In agreement with the previous reports, the mean Raman spectrum of BCC indicates more intense bands corresponding to DNA (e.g. O-P-O symmetric stretching 788 cm^{-1}, PO^{2-} 1098 cm^{-1} and guanine 1577 cm^{-1}), which was attributed to the large number of cells in the BCC regions and their higher nucleus to cytoplasm ratio as supported by the H&E images. While the Raman

spectrum of healthy dermis was dominated by bands specific to collagen fibres (in particular the 851 and 950 cm^{-1} bands assigned to proline and hydroxyproline and the characteristic 1200-1350 cm^{-1} region) [28], the spectra corresponding to the inflamed regions of the dermis indicated a strong contribution from DNA. This finding was in agreement with the H&E images indicating a large number of lymphocytes in the inflamed dermis regions. The Raman spectra of the skin structures rich in lipids, such as sebaceous glands and fat regions, show specific bands characteristic of C-H, C-C and C=C vibrations (850cm^{-1}, 1070cm^{-1}, 1267cm^{-1}, 1301cm^{-1}, 1450cm^{-1}, ~1660cm^{-1}) [27]. In addition to the Raman bands associated with lipids, the spectra of the sebaceous glands also indicated few bands assigned to proteins (e.g. 1003 cm^{-1} band assigned to phenylalanine).

Based on the differences observed in the Raman spectra of the BCC and healthy skin, two spectral classification models using linear discrimination analysis (LDA) were developed. Figure 2 shows the schematic of the overall classification model, which consisted of multiple two-class LDA functions. Compared to a single multiclass LDA model, the multiple two-class LDA allows a greater degree of flexibility in controlling the specific decision boundaries for each skin structure [17,29]. The classification models required a data reduction technique to ensure that the number of spectral features used as input in the LDA was smaller than the total number of spectra in the database. The performance of the classification models was evaluated in terms of classification accuracy and inter-instrument variability. Although an objective quantification of the performance classification models requires the use of an independent test dataset (see Section 3.2), the sensitivity and specificity of the models were calculated using a stratified random sub-sampling 4:1 (80-20%) cross-validation repeated 100 times.

The first method of data reduction was principal component analysis (PCA), which has been extensively used in conjunction with LDA for imaging and diagnosis of various cancers [18].

When the Raman spectra from each instrument were analysed individually, the classification accuracy of the LDA using the scores from the first 13 principal components was 93±3 % sensitivity and 95±5 % specificity for the discrimination of BCC. However, these values dropped to 90±3 % sensitivity and 93±5 % specificity when the datasets from the two instruments were mixed. The decrease in the classification accuracy was caused by small shifts in the wavenumber axis (~0.5cm^{-1}) of the two instruments.

The second method for data reduction was the selection of spectral features (band intensity and frequency) based on the inspection of the mean Raman spectra corresponding to BCC and the other skin structures, as well as their computed differences. These spectral features are intended to discriminate the classes of interest and are directly associated with intrinsic molecular differences between classes. To reduce the inter-instrument errors and variations in band intensities I due to fluctuations in laser power or sampling protocols, the spectral features were represented in the form of the following R_i (i=1-13) features representing intensity ratios and band frequencies:

$$R_1 = \frac{I_{788}}{I_{1003}}, \qquad R_2 = \frac{I_{820}}{I_{1003}}, \qquad R_3 = \frac{I_{853}}{I_{1003}}, \qquad R_4 = \frac{I_{930}}{I_{1003}},$$

$$R_5 = \frac{I_{848}}{I_{1003}}, \qquad R_6 = \frac{I_{940}}{I_{1003}}, \qquad R_7 = \frac{I_{1082}}{I_{1003}}, \qquad R_8 = \frac{I_{1459}}{I_{1660}},$$

$$R_9 = \frac{I_{1577}}{I_{1003}}, \qquad R_{10} = \frac{I_{1312}}{I_{1268}}, \qquad R_{11} = \frac{I_{1300}}{I_{1265}}$$

$$R_{12} = \text{Central Position } 1490 \text{ cm}^{-1} \text{ band}, \qquad R_{13} = \text{Central Position } 1665 \text{ cm}^{-1} \text{ band}$$

where I represent the intensities of the Raman bands at wavenumber indicated by the subscript. R_1-R_9 are distinctive spectral features for DNA and collagen, R_{10} describes the amide III spectral region which provides a good classification for collagen while R_{11}-R_{13} are

selected to identify the skin structures rich in lipids. Table 1 presents the classification results as a confusion matrix, in which each off-diagonal entry (i, j), $i \neq j$, of this matrix is the rate of error of misclassifying class i as class j, whereas each diagonal entry is the sensitivity for class i, i.e. the rate of classifying this class correctly. The LDA classification model based on the 13 selected spectral features was able to discriminate BCC from healthy tissue (taken as all of the other classes combined) with 90±4 % sensitivity and 97±2 % specificity at a 95% target sensitivity (the classifier was applied in the regime corresponding to 95% sensitivity on the training dataset). Although the classification accuracies for BCC obtained from the two models were similar, the model using the selected spectral features was preferred because of the supervised selection the Raman spectral features used for the classification and lower susceptibility to inter-instrument variations.

3.2 Raman spectral histopathology for skin tissue sections

As a first step to objectively evaluate the performance of the Raman spectral model to accurate locate and discriminate BCC, the classification model was applied on independent tissue sections (20 μm thickness) obtained from new patients during MMS. Compared to tissue blocks where the histopathology diagnosis can be carried out only on adjacent sections due to changes in the shape of the tissues during sectioning, the H&E staining can be performed on the same tissue sections used for Raman spectral analysis as no further sectioning was required. Therefore a direct comparison between the H&E and spectral images can be carried out to quantify the performance of the spectral classification model.

Pseudo-colour images providing automated diagnosis of BCC were built by applying the LDA model using the 13 selected spectral features R_j (j=1-13) on the Raman maps. The Raman spectral images containing the diagnosis were based entirely on the classification model without supervision from the user. Examples of spectral images for 20 μm thick

sections cut from tissue layers are presented in Figure 4 along with their corresponding H&E images. The spectral images for these independent samples show a good agreement with the H&E images as well as a high accuracy of the LDA classification model. Figure 4A represents a skin section containing nodular BCC, hair follicles and dermis. All these structures were correctly classified by the LDA model, although small regions of inflamed dermis containing large number of lymphocytes and few basal layer regions around hair follicles were classified as BCC. However, the majority of the lymphocytic inflamed dermis was correctly classified. It is worth noting that the sensitivity for detection of BCC is indeed high as BCC regions as small as 40×40 μm^2 were detected. Figure 4B is another example of a skin section containing nodular BCC, epidermis, hair follicles and dermis, confirming that the correlations of the RMS and H&E images was high. Only small regions of basal layers at the edges of the hair follicles were misclassified as BCC.

While Figures 4A and B show cases of tissue sections with nodular BCC for which diagnosis by H&E staining was straightforward, Figure 4C is an example of a skin section for which the diagnosis based on the H&E image is difficult without an evaluation of adjacent H&E stained sections. The H&E image shows three regions (indicated with arrows) which appear morphologically similar to BCC, several hair follicles and regions of inflamed dermis. After tissue sectioning and evaluation of sequential layers, the tissue sample was diagnosed as negative (BCC-free) and the potential BCC regions were assigned as hair follicles. The unsupervised LDA model based on the Raman spectra provided the correct diagnosis based only on the molecular information in the examined tissue section without requiring the evaluation of adjacent sections: the tissue was diagnosed as BBC-negative and all hair follicle regions were correctly classified.

Since the samples used for spectral imaging were independent from the samples included in the classification model, a more objective evaluation of the classification performance can be

obtained by comparing the ground-truth label obtained from the H&E images and the predicted label from the result of LDA classification. To obtain the ground truth label, after the unsupervised two-stage-*k*-means clustering on the Raman spectra of the tissue sections, each cluster was labelled from the corresponding H&E image. Based on this test, the overall sensitivity for discrimination of BCC was 100% (all BCC were correctly detected). On the other hand, due to the misclassification of the small areas of inflamed dermis and basal layers, the specificity for BCC was 97.5%. While the specificity value is similar to the value calculated by cross-validation of the spectral model dataset, the sensitivity was significantly higher. Although the higher sensitivity could be attributed partly to the lower number of spectra in the tissue sections, this estimation provides an objective validation of the spectral classification model.

3.3 Raman spectral imaging and diagnosis for tissue blocks

The results in Section 3.2 show that the spectral LDA model can provide accurate classification of the skin structures and diagnosis of BCC in thin tissue sections, based entirely on the chemical composition of the tissue and without requiring evaluation of adjacent sections. We subsequently tested whether the Raman spectral classification model maintained the same levels of classification accuracy when examining thicker tissue layers and blocks removed during MMS without sectioning. If an accurate and objective evaluation of the tumour margins can be obtained by examining only the bottom surface of the excised tissue blocks without sectioning and preparation of frozen sections (~45 minutes on average), these time-consuming procedures would no longer be required.

Figure 5 presents examples of images and unsupervised classification using the LDA spectral model for typical tissue blocks along with the corresponding H&E images of the adjacent sections. The samples are independent from the tissues used for the development of the

model as they were collected from new patients. Figure 5A shows that the spectral image and the diagnosis are in good agreement with the H&E histopathology and the large nodular BCC in the centre of the block is correctly diagnosed. High classification accuracy and BCC diagnosis was also observed in the case of tissue blocks containing superficial and infiltrative BCC (Figures 5B and C). The tissue structures found in healthy skin (epidermis, dermis, hair follicles and the sebaceous glands) are also correctly classified in most cases. Figure 5D shows a typical example of BCC-negative tissue blocks, in which case the diagnosis provided by the spectral classification model was correct. In certain cases (e.g. Figure 5A), errors caused by poor contact between the edges of the tissue and the coverslip led to poorer quality Raman spectra and therefore low classification accuracy. However, such errors may be eliminated by future optimisation of the instrumentation and do not represent a limitation of Raman spectroscopy technique.

3.4 Spectral imaging and automated diagnosis of tissue blocks by selective sampling

The main aim of this study was to explore the potential for developing multivariate classification models for imaging and diagnosis of BCC in skin tissues based on their intrinsic molecular properties as obtained from Raman spectroscopy measurements. To achieve this aim, the spectral data was acquired by raster scanning the samples through the laser spot, ensuring objectivity in the data collection. While this sampling method has allowed the identification of the spectral features which can be used for developing high-accuracy classification models, the raster scanning procedure requires acquisition time of ~1.4 hours per 1 mm^2 (integration time 2sec/site, 20μm step size), making it impractical for use during tissue-conserving surgery. However, it is worth noting that once the model has been developed, the measurement of the Raman spectra of new tissue samples does not

require raster scanning. There are several alternative Raman micro-spectroscopy techniques which have been developed recently for faster acquisition of spectral maps of tissues. For example, spectral imaging by laser-line scanning can speed up the acquisition by a factor of 10× while maintaining the same level of diagnosis accuracy [30]. This technique relies on expanding the excitation laser in a line to allow simultaneous acquisition of Raman spectra from different regions of the sample [30]. Coherent anti-Stokes Raman scattering (CARS) and stimulated Raman scattering (SRS) have been reported recently to image tissues, including skin, at speeds as high as video rate [31,32]. Although these techniques have certain limitations in terms of spectral accuracy, further future developments and potential implementation of the spectral models reported in this study may provide a viable approach for fast imaging and automatic diagnosis of BCC during MMS.

In this part we present an illustration of using the spectral classification model developed in this study in conjunction with a novel selective-sampling technique [26] to allow the acquisition of images and diagnosis of BCC in tissue blocks within ~30 minutes (tissue area limited by our equipment to 5×5 mm^2). In this technique the sampling points were selected in real-time based on the classification scores of each individual spectrum, as analysed by the LDA model described in Section 3.1.

An example of a Raman spectral image and automated diagnosis for a tissue block acquired by integrating the LDA classification model with the selective scanning is presented in Figure 6. The diagnosis was made with the unsupervised two-stage-*k*-mean-LDA method discussed in Section 2.3 and the final reconstructed image was computed by the nearest-neighbour method. Compared to the gold-standard H&E image, the Raman spectral image achieved a good level of accuracy in the discrimination of BCC, considering that the overall time for its acquisition was ~35-fold shorter than the time required for raster-scanning. Figure 6C shows the distribution of the sampling points which confirms that the selective sampling algorithm

led to a higher sampling density in the regions where the chemical heterogeneity of the sample was higher, in particular at the boundaries of the BCC regions.

CONCLUSIONS

In this study we investigated whether Raman micro-spectroscopy can be used in an unsupervised manner to obtained images and diagnose tumours at the surface of tissue blocks excised during tissue-conserving surgery. The main aim was to achieve objective and accurate diagnosis of the tissues without tissue sectioning or other sample preparation methods. Although this technique is not limited to skin, the focus of the study was on detection of basal cell carcinoma (BCC) in tissue layers excised during Mohs micrographic surgery (MMS). A classification model based on Raman spectra collected from skin samples from 65 patients achieved a sensitivity of 90±4% and specificity of 97±3% in a 4:1 cross-validation. The classification model was based on selected Raman bands which were associated with intrinsic chemical differences between BCC and other tissue structures found in healthy skin. An objective evaluation of the technique was obtained by applying the classification model on tissue sections and blocks from new patients. In all cases, an excellent agreement between the spectral images/classification and the gold-standard histopathology was achieved. BCC was detected in all tissue samples, including samples with nodular, superficial and infiltrative BCC. Although the raster scanning method used for data acquisition requires long imaging times which are impractical for intra-operative use, we used the spectral classification model in conjunction with a recently developed selective sampling technique to show that unsupervised diagnosis and imaging of BCC can be obtained in ~30 minutes for tissue samples as large as 5×5 mm^2. However, integration of the spectral models reported in this study with other Raman micro-spectroscopy techniques using even faster sampling techniques (e.g coherent anti-Stokes Raman spectroscopy or stimulated Raman spectroscopy) may reduce the imaging times to only few minutes, which would make this technique suitable for intra-operative evaluation of tumour margins.

While the focus of this study has been on developing Raman spectroscopy models for MMS, its application to patients with less complicated BCC removed by straightforward excision could transform the way all BCC surgery is performed by providing an immediate answer on whether the excised tissue is clear.

GRANT SUPPORT

This paper presents independent research commissioned by the National Institute for Health Research (NIHR) under its Invention for Innovation (i4i) Programme (grant number II-AR-0209-10012). The views expressed are those of the author(s) and not necessarily those of the NHS, the NIHR or the Department of Health.

References (for authors >6, et al)

1. Nouri K, Skin Cancer: McGraw-Hill Medical. Vol. 1 Edition; 2007.

2. NICS. Improving outcomes for people with skin tumours including melanoma. 2006 [cited 2006; Available from: http://www.nice.org.uk/nicemedia/live/10901/28906/28906.pdf.

3. CancerResearchUK. Types of skin cancer. 2011; Available from: http://cancerhelp.cancerresearchuk.org/type/skin-cancer/about/types-of-skin-cancer.

4. McGovern TW, Leffell DJ, Mohs surgery - The informed view. Arch Dermatol 1999; 135(10): 1255-1259.

5. Telfer NR, Colver GB, Powers PW. Guidelines for the management of basal cell carcinoma. Brit J Dermatol 1999; 141(3): 415-423.

6. Leibovitch I, Huilgol SC, Selva D, Richards S, Paver R. Basal cell carcinoma treated with Mohs surgery in Australia - II. Outcome at 5-year follow-up. J Am Acad Dermatol 2005; 53(3): 452-457.

7. Mosterd K, Krekels GAM, Nieman FHM, Ostertag JU, Essers BAB, Dirksen CD, et al. Surgical excision versus Mohs' micrographic surgery for primary and recurrent basal-cell carcinoma of the face: a prospective randomised controlled trial with 5-years' follow-up. Lancet Oncol 2008; 9(12): 1149-1156.

8. Rowe DE, Carroll RJ, Day CL. Long-term recurrence rates in previously untreated (primary) basal-cell carcinoma- implications for patient follow-up. J Dermatol Surg Onc 1989; 15(3): 315-328.

9. Mogensen M, and Jemec GBE, Diagnosis of nonmelanoma skin cancer/keratinocyte carcinoma: A review of diagnostic accuracy of nonmelanoma skin cancer diagnostic tests and technologies. Dermatol Surg 2007; 33(10): 1158-1174.

10. Raab SS, Grzybicki DM. Quality in cancer diagnosis. Ca Cancer J Clin 2010; 60(3): 139-165.

11. Brochez L, Verhaeghe E, Grosshans E, Haneke E, Pierard G, Ruiter D, et al. Inter-observer variation in the histopathological diagnosis of clinically suspicious pigmented skin lesions. J Pathol 2002; 196(4): 459-466.

12. Krahl D, Sellheyer K. Monoclonal antibody Ber-EP4 reliably discriminates between microcystic adnexal carcinoma and basal cell carcinoma. J Cutan Pathol 2007; 34(10): 782-787.

13. Kist D, Perkins W, Christ S, Zachary CB. Anti-human epithelial antigen (Ber-EP4) helps define basal cell carcinoma masked by inflammation. Dermatol Surg 1997; 23(11): 1067-1070.

14. Tellechea O, Reis JP, Domingues JC, Baptista AP. Monoclonal- antibody Ber-EP4 distinguishes basal-cell carcinoma from squamous-cell carcinoma of the skin. Am J Dermatopath 1993; 15(5): 452-455.

15. Haka AS, Shafer-Peltier KE, Fitzmaurice M, Crowe J, Dasari RR, Feld MS. Diagnosing breast cancer by using Raman spectroscopy. P Natl Acad Sci USA 2005; 102(35): 12371-12376.

16. Huang Z, Teh SK, Zhen W, Mo J, Lin K, Shao X, et al. Integrated Raman spectroscopy and trimodal wide-field imaging techniques for real-time in vivo tissue Raman measurements at endoscopy. Opt Lett 2009; 34(6): 758-760.

17. Larraona-Puy M, Ghita A, Zoladek A, Perkins W, Varma S, Leach IH, et al. Development of Raman microspectroscopy for automated detection and imaging of basal cell carcinoma. J Biomed Opt 2009; 14(5): 054031.

18. Nijssen A, Schut TCB, Heule F, Caspers PJ, Hayes DP, Neumann MHA, et al. Discriminating basal cell carcinoma from its surrounding tissue by Raman spectroscopy. J Invest Dermatol 2002; 119(1): 64-69.

19. Almond LM, Hutchings J, Shepherd N, Barr H, Stone N, Kendall C. Raman spectroscopy: a potential tool for early objective diagnosis of neoplasia in the oesophagus. J Biophotonics 2011; 4(10): 685-695.

20. Tollefson M, Magera J, Sebo T, Cohen J, Drauch A, Maier J, et al. Raman spectral imaging of prostate cancer: can Raman molecular imaging be used to augment standard histopathology? Bju Int 2010; 106(4): 484-488.

21. Stone, N, Matousek P. Advanced transmission Raman spectroscopy: A promising tool for breast disease diagnosis. Cancer Res 2008; 68(11): 4424-4430.

22. Wartewing S. IR and Raman spectroscopy: Fundamental processing: Wiley-VCH; 2003.

23. Pirzer M. Method and device for correcting a spectrum. US Patent. 2008: US.

24. Ly E, Piot O, Durlach A, Bernard P, Manfait M. Differential diagnosis of cutaneous carcinomas by infrared spectral micro-imaging combined with pattern recognition. Analyst 2009; 134(6): 1208-1214.

25. Sebiskveradze D, Vrabie V, Gobinet C, Durlach A, Bernard P, Ly E, et al. Automation of an algorithm based on fuzzy clustering for analyzing tumoral heterogeneity in human skin carcinoma tissue sections. Lab Invest 2011; 91(5): 799-811.

26. Rowlands CJ, Varma S, Perkins W, Leach I, Williams H, Notingher I. Rapid acquisition of Raman spectral maps through minimal sampling: applications in tissue imaging. J. Biophotonics 2012; 1: 1-10.

27. Tu AT. Raman Spectroscopy in Biology: Principles and Applications: Wiley-Blackwell; 1982.

28. Frushour BG, Koenig JL. Raman-scattering of collagen, gelatin, and elastin. Biopolymers 1975; 14(2): 379-391.

29. Larraona-Puy M, Ghita A, Zoladek A, Perkins W, Varma S, Leach IH, et al. Discrimination between basal cell carcinoma and hair follicles in skin tissue sections by Raman micro-spectroscopy. J Mol Struct 2011; 993(1-3): 57-61.

30. Hamada K, Fujita K, Smith NI, Kobayashi M, Inouye Y, Kawata S. Raman microscopy for dynamic molecular imaging of living cells. J Biomed Opt 2008; 13(4).

31. Begin S, Burgoyne B, Mercier V, Villeneuve A, Vallee R, Cote D. Coherent anti-stokes Raman scattering hyperspectral tissue imaging with a wavelength-swept system. Biomed Opt Express 2011; 2(5): 1296-306.

32. Saar BG, Freudiger CW, Reichman J, Stanley CM, Holtom GR, Xie XS. Video-rate molecular imaging in vivo with stimulated Raman scattering. Science 2010; 330(6009): 1368-1370.

Table 1: The confusion matrix for the spectral classification model based on 4:1 cross-validation. The numerical values represent the classification percentages and the standard deviations are showed in brackets.

Predict / True	Unknown	BCC	Epidermis	Inflamed Dermis	Dermis	Fat	Sebaceous Gland	Muscle
Unknown	**0 (0)**	0 (0)	0 (0)	0 (0)	0 (0)	0 (0)	0 (0)	0 (0)
BCC	0 (0.2)	**91 (4)**	5 (3)	1 (1)	3 (2)	0 (0)	0 (0)	0 (0)
Epidermis	0 (0.3)	9 (5)	**84 (7)**	5 (4)	2 (2)	0 (0)	0.2 (0.8)	0 (0.4)
Inflamed Dermis	0 (0)	0 (1)	0 (0)	**85 (16)**	15 (16)	0 (0)	0 (0)	0 (0)
Dermis	1 (1)	2 (2)	0.2 (0.7)	13 (5)	**81 (6)**	0 (0)	0 (0)	2 (2)
Fat	9 (15)	0 (0)	0 (0)	0 (0)	0 (0)	**91 (15)**	0 (2)	0 (0)
Sebaceous Gland	0 (0)	0 (0)	0 (0)	0 (0)	0 (0)	5 (12)	**95 (11)**	0 (0)
Muscle	0 (0)	0 (0)	1 (4)	13 (15)	4 (9)	3 (7)	2 (5)	**78 (18)**

Figure legends

Figure 1. A typical example of using the step-wise *k*-means clustering algorithm for assigning the Raman spectra to the tissue structures and BCC during the development of the classification model. (A) The H&E stained image of the tissue section; (B) Pseudo-colour image obtained by *k*-means clustering of all the Raman spectra; (C) Use of a second *k*-means clustering algorithm only on the spectra contained in the red cluster in (B).

Figure 2. Mean Raman spectra of skin structures: basal cell carcinoma (BCC), epidermis (Epid.), hair follicle (Hfol.), muscle (Mus.), inflamed dermis (Inf. D), dermis (Derm), fat, sebaceous glands (Seb. G.).

Figure 3. Schematic of the linear discriminant analysis (LDA) classification model.

Figure 4. Comparison between the histopathology H&E images (left) and the unsupervised Raman spectral images for typical tissue sections. The scale bar in (A) applies to all images.

Figure 5. Examples of unsupervised Raman spectral images for tissue blocks along with the histopathology H&E images of adjacent sections: (A) nodular BCC; (B) superficial BCC; (C) infiltrative BCC; (D) skin sample with no BCC.

Figure 6. Example of a unsupervised Raman spectral image obtained by selective sampling. (A) The H&E image of the adjacent section; (B) Reconstructed Raman spectral image; (C) The distribution of the sampling points.

Figures

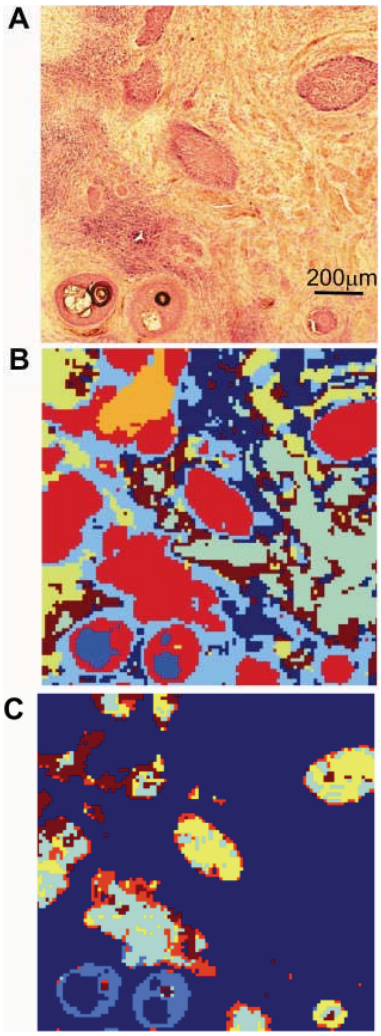

Figure 1

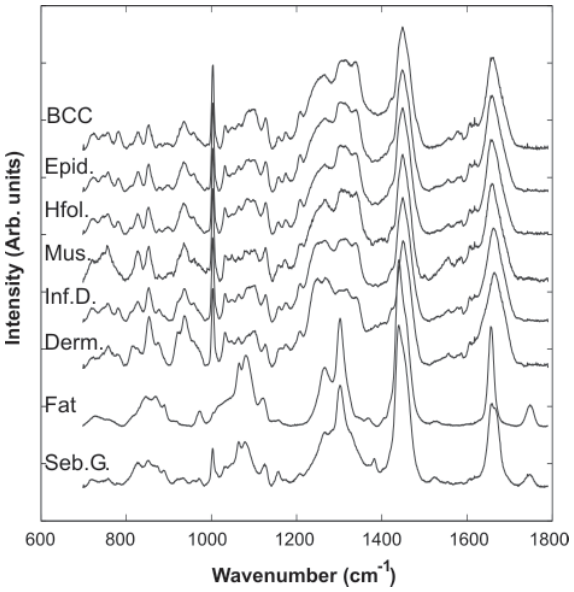

Figure 2

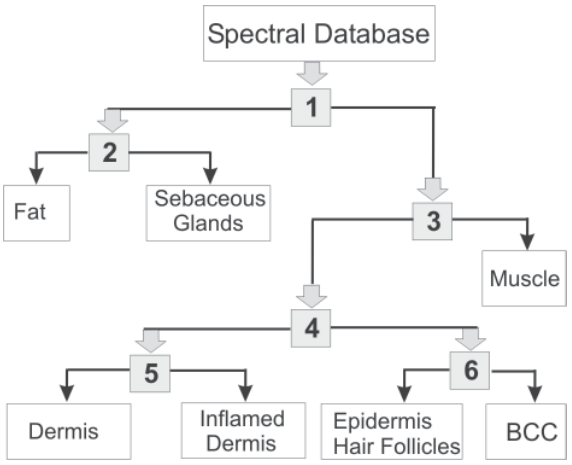

Figure 3

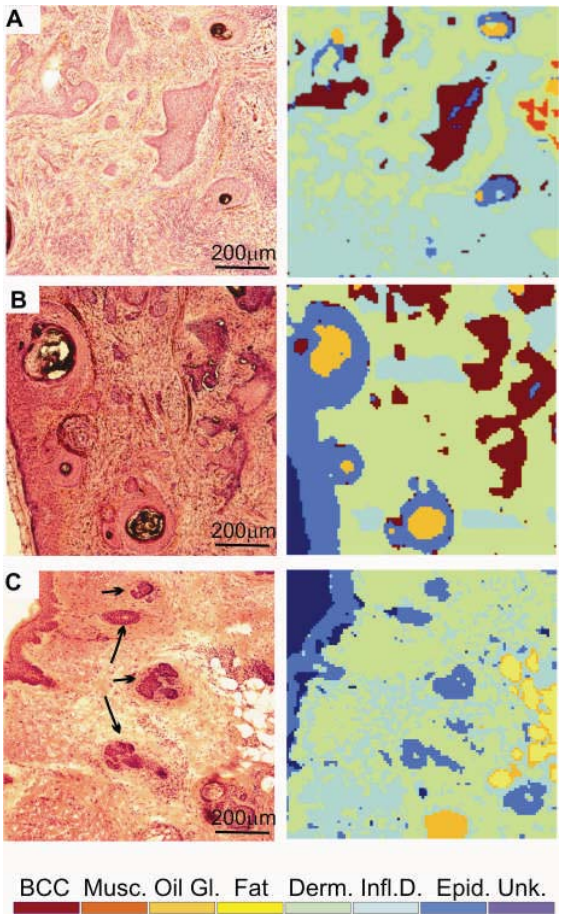

Figure 4

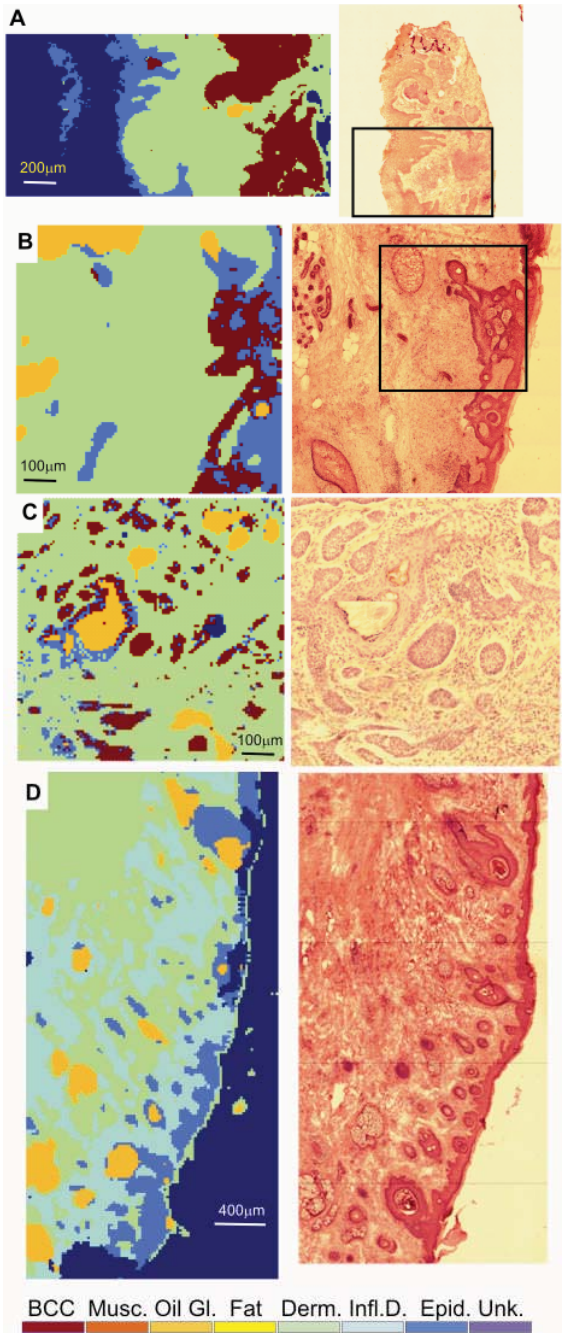
A
200µm
B
100µm
C
100µm
D
400µm
BCC Musc. Oil Gl. Fat Derm. Infl.D. Epid. Unk.

Figure 5

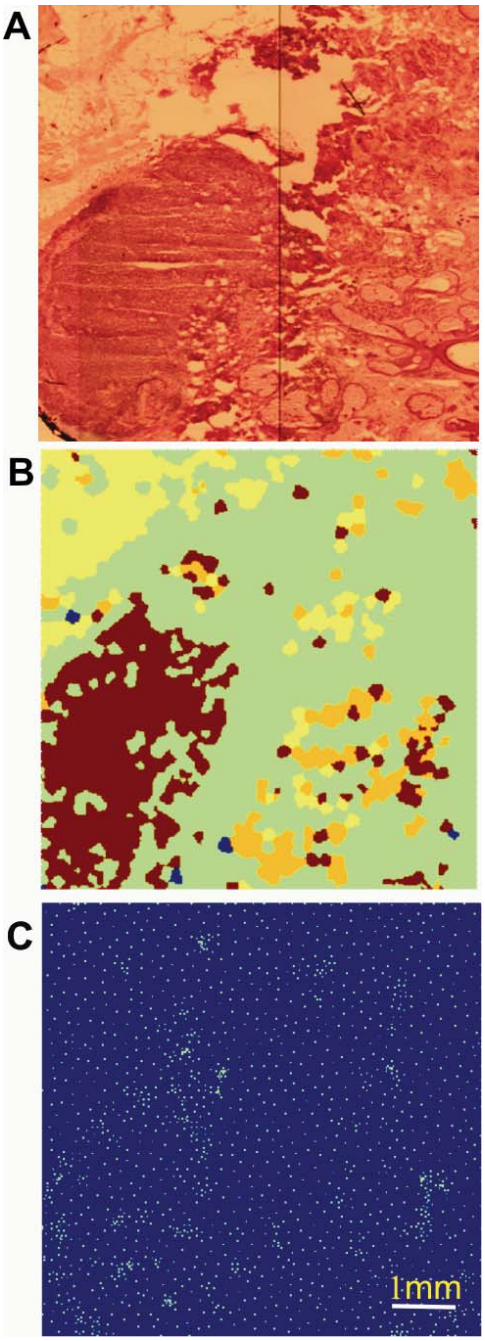

Figure 6.